Neutral-ion interaction in the auroral *E* region obtained from coordinated Fabry-Perot imager and VHF radar observations

T. Sakanoi,[1] H. Fukunishi,[1,2] K. Igarashi,[3] S. Okano,[1] and N. Nishitani[4]

Received 1 December 2008; revised 8 May 2009; accepted 7 July 2009; published 23 September 2009.

[1] It is important to investigate the small-scale dynamics of thermospheric neutrals and ionospheric plasmas at high latitudes since there are local and temporal variations in energy input and transfer processes associated with auroral activities. To clarify these ionosphere-thermosphere interactions in the auroral *E* region, we examined neutral winds and plasma motions obtained by coordinated Fabry-Perot imager and VHF radar observations at Syowa Station, Antarctica. From case studies on 11 and 12 September 1996, we found a good correlation between temporal variation (period < 1 hr) of *E* region neutral winds measured by the Fabry-Perot imager and the Doppler velocities of plasmas obtained from the VHF radar echoes. On the other hand, the absolute mean values of the neutral winds were around zero whereas the plasma Doppler velocities were 350–400 m/s, showing a significant discrepancy. Considering that the neutral-ion and ion-neutral momentum transfer collision frequencies in the *E* region are $\sim 10^{-6}$ Hz and $\sim 10^{2}$ Hz, respectively, these good correlations are probably due to ion motions driven by neutral drag force, suggesting a strong coupling between neutrals and ions in the *E* region. The observed correlation and discrepancy between the radar Doppler velocity and the neutral wind velocity are consistent with the linear theory of *E* region irregularities that shows the radar Doppler velocity is the sum of two components; one is the $\mathbf{E} \times \mathbf{B}$ drift speed, and another is proportional to the neutral wind velocity.

Citation: Sakanoi, T., H. Fukunishi, K. Igarashi, S. Okano, and N. Nishitani (2009), Neutral-ion interaction in the auroral *E* region obtained from coordinated Fabry-Perot imager and VHF radar observations, *J. Geophys. Res.*, *114*, A09305, doi:10.1029/2008JA013956.

1. Introduction

[2] At high latitudes, ionosphere-thermosphere (IT) interaction processes show complicated behaviors indicating significant temporal and spatial variations associated with auroral activities, and neutral-ion (NI) coupling plays a key role in the IT interactions. The ion motion is mainly controlled by the ionospheric electric field from the magnetosphere, but it is also affected by neutral particles driven by Joule and particle heatings, and an ion drag force [e.g., *Fujii et al.*, 1998a]. These driving forces of ions and neutrals are dramatically enhanced during auroral substorms and produce a strong and complicated NI coupling [*Deng et al.*, 1991]. Since local (~tens of km) and temporal (less than ten min) variations of the ionospheric electric field and auroral particle precipitations exist during substorms [e.g., *Conde et al.*, 2001], the NI coupling essentially shows such local and temporal behaviors. Thus it is necessary to investigate the small-scale variations in neutral and ion motion in association with auroral activities in order to gain an understanding of the response of auroral inputs to the thermosphere and the ionosphere and its energy transfer.

[3] There have been a number of studies on the high-latitude NI coupling have using ground-based, satellite and rocket measurements, and computer simulations. In particular, DE-2 satellite measurement data have contributed to reveal the large-scale interaction between neutrals and ions in the high-latitude thermosphere along the satellite track [e.g., *Killeen et al.*, 1985; *Killeen and Roble*, 1988]. The global aspects of high-latitude thermospheric dynamics have also been examined by using general circulation models [e.g., *Deng et al.*, 1993; *Fuller-Rowell et al.*, 1994; *Ridley et al.*, 2003; *Wang et al.*, 2006]. Ground-based observations have proved useful for examines the local and temporal variations of the NI coupling. The horizontal distributions of neutral winds and temperatures at the altitudes of the auroral emission layers have been measured by an all-sky Fabry-Perot interferometer (FPI), and they showed temporal variations associated with auroral variations [e.g., *Rees et al.*, 1991; *Conde and Smith*, 1998, *Ishii et al.*, 1999; *Cierpka et al.*, 2000; *Kosch et al.*, 2001; *Aruliah et al.*, 2005]. Incoherent scatter radar data have yielded precise vertical profiles of plasma and neutral parameters. In particular, *Fujii et al.* [1998b] used EISCAT radar data to estimate the energy transfer in the NI coupling system

[1]Graduate School of Science, Tohoku University, Sendai, Japan.
[2]Japan Society for the Promotion of Science Beijing Office, Beijing, China.
[3]National Institute of Information and Communications Technology, Koganei, Japan.
[4]Solar-Terrestrial Environment Laboratory, Nagoya University, Nagoya, Japan.

0148-0227/09/2008JA013956$09.00

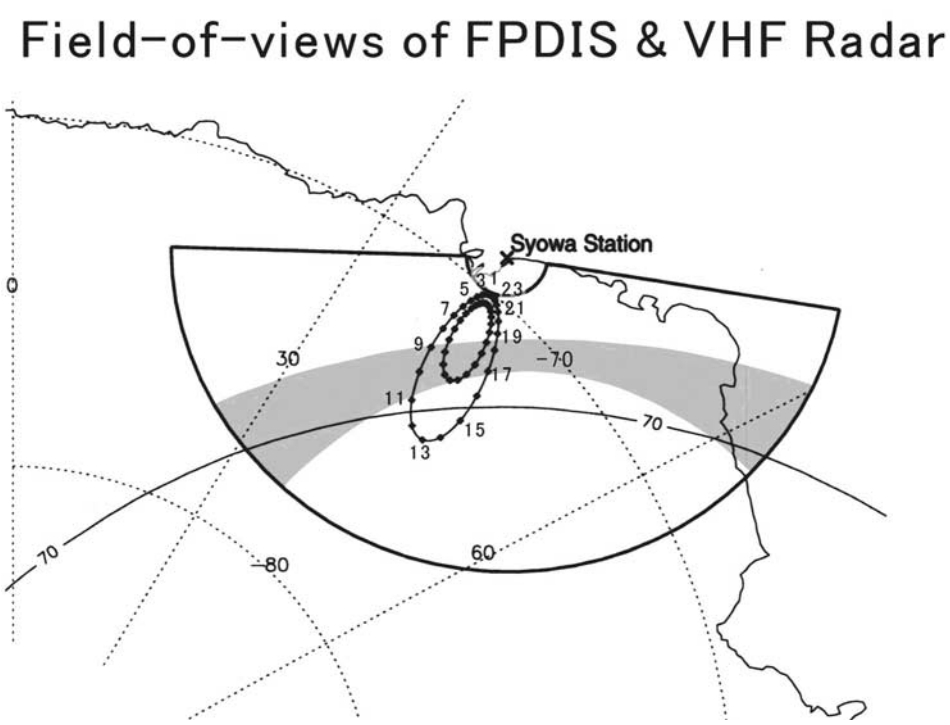

Figure 1. Geographical map showing the FOVs of the FPDIS and VHF radar. Fan-shaped solid lines show the FOV of the VHF radar, and the *E* region echoes are mostly obtained in the hatched region where the raypaths transmitted from the radar are almost perpendicular to the geomagnetic field. Inner and outer fringes of the FPDIS are mapped, and fringe directions are indicated at the side of the fringes. Invariant latitudes are drawn as solid curves.

quantitatively. Despite the above studies, the local and temporal NI couplings are still not well understood since few simultaneous measurements of neutrals and ions have been carried out in the auroral region. Recently, *Sakanoi et al.* [2002] used FPI and HF radar measurements to obtain temporal relationship between neutral winds and ion drifts in the auroral *F* region. Nevertheless, the NI coupling in the *E* region is expected to be quite different from the one in the *F* region since the ion-neutral momentum transfer collision frequency in the *E* region is much ($\sim 10^2$ times) greater than that in the *F* region [*Schunk and Nagy*, 1980, 2000; *Thayer*, 1998].

[4] In this study, we focused on the local interaction between neutrals and ions in the auroral *E* region, as ascertained from spatially resolved neutral wind and plasma drift data measured by a Fabry-Perot Doppler imaging system (hereafter, FPDIS) and auroral VHF radar at Syowa Station, Antarctica (69.0° S and 39.6° E in geographic coordinates and 66.4° in magnetic latitude). These imaging measurements of neutral winds and plasma drifts provided us with a unique opportunity to examine the local IT coupling processes in the auroral *E* region. Since the typical spatial resolutions of neutral and plasma drift measurements were made at tens of km, these data can contribute to evaluating the effects of small-scale variations on the parameters of the global thermosphere ionosphere general circulation models.

2. Instrumentation and Data Analysis

2.1. Fabry-Perot Doppler Imaging System

[5] The FPDIS measured the Doppler shift and width of auroral OI 557.7 emissions by using an interference filter whose center wavelength and full width half maximum were 558.1 nm and 0.9 nm, respectively. The peak altitude of the OI 557.7-nm emission was assumed to be 120 km, and the validity of this assumption is discussed later in section 4.1. The field-of-view (FOV) of the FPDIS was set to be 42°by using a combination of a wide-angle objective lens and a slant mirror in the front of the objective lens in order to observe neutral winds and temperatures in the *E* regions covered by the VHF radar. Figure 1 is a map of the observation geometry showing the FOVs of the FPDIS and VHF radar.

[6] Since the detailed instrumentation of the FPDIS and the method of data analysis are described by *Sakanoi et al.* [2002] and *Nakajima et al.* [1995], only a brief description of them will be given here. Incident auroral light interferes at the 116-mm aperture Fabry-Perot etalon, and over two orders of interference fringes are finally focused on the imaging sensor. A fringe image is transformed into 48 sliced fringe profiles (24 for each of the inner and outer fringes). A Gaussian fitting is performed on each fringe profile to estimate the Doppler shift of the auroral emissions, while a numerical technique based on a truncated Fourier series is used to estimate the Doppler broadening. Thus the line-of-sight (LOS) velocities and temperatures of neutrals can be estimated at 48 points on the sky since the fringe image is conjugate with the field-of-view on the sky. The time resolution of the OI 557.7-nm data was dependent on auroral intensity and was in the range of 30 s to 10 min. He-Ne (632.8 nm) laser fringe data are routinely obtained every 1-h to calibrate the FPDIS's instrumental functions, such as etalon spacing drift. Furthermore, the reference fringe position for the

wind-zero velocity was determined from a "cloudy" fringe image. The cloudy data were obtained during several nights in 1996 when the sky was uniformly cloudy and auroral activity was low. The uniformity of cloud was monitored by the auroral all-sky camera at Syowa. To validate the cloudy data, we produced wind-zero fringe data for each cloudy night, and compared them. Since these cloudy data were found to be comparable, it is suggested that the light is scattered sufficiently by clouds and these data are not affected by local and temporal variations. Finally, the most representative (median) cloudy fringe data was chosen to be the wind-zero fringe. Errors in the relative variations of neutral winds and temperatures are estimated to be better than 15 m/s and 80 K, respectively, although significant offsets (∼200 K) seem to be involved in the absolute values of temperature. We excluded the data obtained during periods when the auroral intensity distribution showed a steep gradient in the FOV of the FPIDS, since the steep intensity gradient would produce the apparent shift of fringe peak position, that is, errors in wind velocity. In addition, we only used the data for periods when room temperature remained stable since a complicated etalon drift tended to occur when room temperature varied by more than 5 K/hour.

2.2. Auroral VHF Radar

[7] Observations of radio auroral echoes generated by *E* region irregularities in the altitude range of ∼110 km have been carried out using the auroral VHF radar at Syowa station since 1966 [*Igarashi et al.*, 1995; *Ogawa*, 1996]. In 1995, a 50-MHz scanning-beam VHF auroral radar with two sets of array antennas was installed in order to cover the whole echo region. The Syowa VHF radar scans a wide area in the range from 120 to 1000 km with a FOV of ∼170° centered on geomagnetic south, of which the azimuthal angle from geographic north is 131.2°. In the normal operation mode, one full scan is performed in 4 minutes. The azimuthal beam width of each radar beam is ∼5° and the scan area is divided into 35 azimuthal sectors. The radar transmits a 100-μs pulse (range resolution of 15 km) with a pulse repetition frequency of 667 Hz (maximum unaliasing Doppler velocity of ±500m/s). *E* region echoes mainly come from the hatched region in Figure 1, where the aspect angle is almost zero, namely, where raypaths transmitted from the radar are almost perpendicular to the geomagnetic field.

[8] One of the important functions of the Syowa VHF radar is to regularly observe the Doppler velocity and echo patterns in the *E* region by using the double-pulse technique. The observed Doppler velocity is almost equal to the electron $\mathbf{E} \times \mathbf{B}$ drift velocity when the $\mathbf{E} \times \mathbf{B}$ drift speed is less than the ion acoustic speed, while the observed Doppler velocity saturates at the ion acoustic speed when the $\mathbf{E} \times \mathbf{B}$ drift speed exceeds the ion acoustic speed of ∼400 m/s [*Nielsen and Schlegel*, 1985; *Nielsen et al.*, 1988; *Tanaka and Venkateswaran*, 1982a, 1982b; *Haldoupis and Nielsen*, 1989; *Schlegel*, 1996]. Hereafter, we simply refer to the Doppler velocity obtained from the VHF radar data as "the radar Doppler velocity."

3. Observations

[9] The FPDIS and VHF radar were simultaneously operated on six nights in September 1996. We made detailed case studies of the neutral wind, temperature, and radar Doppler velocity on two of these nights, in which strong echoes were obtained for several hours under clear sky conditions. We also determined the IMF conditions from WIND or IMP8 data in which the time was corrected to take into account solar wind velocities and the distance between the spacecraft and the Earth.

[10] In this paper, we will deal with LOS velocity maps of neutral winds and radar Doppler velocities, since the FPDIS and VHF radar observed in the LOS direction, and therefore we can compare neutral winds with plasma drifts without having to make any further assumptions. Here the horizontal neutral wind was obtained as $U_{LOS}/\sin(\theta)$, where U_{LOS} is the line-of-sight component to of the neutral winds, and θ is the zenith angle, assuming that the vertical wind velocity is negligibly small.

3.1. 12 September 1996 Case

[11] Auroral activities were the intense on the night of 12 September. The K_p values were in the range between 3 and 5. As shown in Figure 2, the WIND satellite data showed mostly negative variations in the IMF Bz component (0 to −4 nT) throughout the night, while the solar wind speeds Vx were relatively high (−600 to −700 km/s). Figure 3 summarize the FPDIS, VHF radar, auroral, and geomagnetic data gathered on this night. Auroral keograms obtained with meridional scanning photometers (MSP) indicated that stable 630-nm and 557.7-nm auroral emissions existed in the poleward direction before 1900 UT, and these moved equatorward from 1900 to 2000 UT. Note that UT is almost the same as magnetic local time (MLT) at Syowa Station. A negative bay of the geomagnetic H component occurred around 1940 UT. The first auroral breakup occurred at ∼2110 UT, as identified by the auroral poleward expansion and the steep negative excursion of the geomagnetic H component. It was followed by the appearance of a pulsating aurora from ∼2145 to 2310 UT. The second breakup occurred at ∼0007 UT on 13 September, followed by the appearance of a pulsating aurora after ∼0020 UT.

[12] As seen in Figure 3 (bottom), the observation room's temperature variations were rather small (maximum of 2.1 K/hour from ∼1900 to 2000 UT). Thus the effect of etalon spacing drift on neutral wind measurements could be satisfactorily corrected. The third and fourth panels in Figure 3 plot the time variations of the neutral winds and radar Doppler velocities, and neutral temperature at the selected locations. (These selected locations are shown in the legends.) Hereafter, to plot the time series of radar Doppler velocity, we show the average of radar Doppler velocities at 9 data points (∼45 × 60 km) centered on the location closest to the FPDIS data point. This averaging is needed since the echo area of the VHF radar was sometimes limited. Figure 4 summarizes neutral winds and radar Doppler velocities superposed on the 557.7-nm auroral images. Note that only selected plots are displayed in Figure 4. The neutral wind data in Figures 3 and 4 indicate that the LOS velocities of horizontal winds were away from Syowa Station before ∼1900 UT. Considering that the FOV of the FPDIS was directed magnetic south-westward and that the MLT was in the premidnight sector, the LOS velocities of horizontal winds away from Syowa represent sunward winds. The Doppler velocities obtained from VHF radar data showed a similar tendency before ∼1900 UT. In

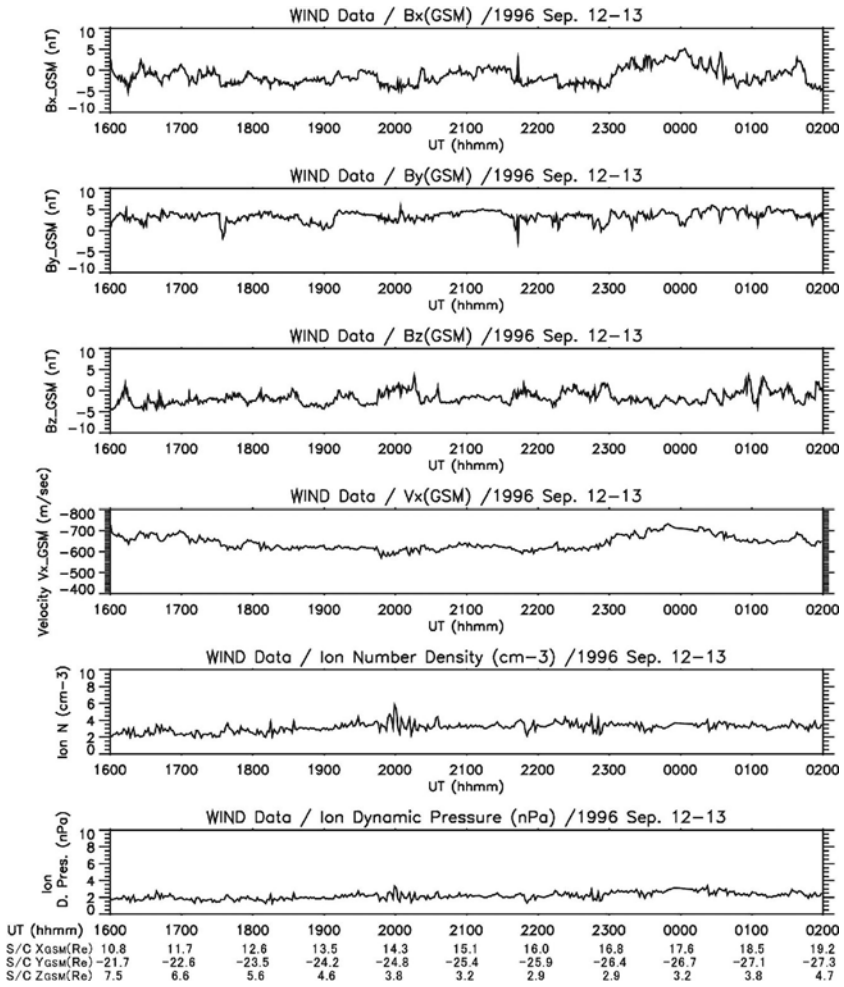

Figure 2. Solar wind conditions measured by the WIND satellite on 12–13 September of 1996.

particular, the velocity distribution map at 1838:02 UT in Figure 4 is consistent with a sunward flow pattern. Since the MSP data show that the FOVs of the FPDIS and VHF radar covered the equatorward region of the auroral oval, the directions of the neutral winds and radar Doppler velocities are consistent with the two-cell pattern of global ionospheric plasma convection. Furthermore, corresponding to the equatorward movement of the aurora from ~1900 to 2000 UT, the neutral winds away from Syowa (−200 to −400 m/s) decelerated, and subsequently attained mostly positive values (less than ~100 m/s). During the same period, the radar Doppler velocities changed direction from about −200 m/s (away from Syowa) to +200 m/s (toward Syowa). The changes in direction of radar Doppler velocities and neutral winds are clearly seen in Figure 4, if we compare the velocity distribution maps at 1836 UT and at 1943 UT, although the neutral wind velocities in the region close to Syowa were still directed away from Syowa as indicated by the red arrows. Thus the plasma convection reversal probably took place during this period, and the neutral winds might have been driven by the ion drag force.

[13] Figures 3 and 4 show that there were oscillations in the neutral winds and temperatures with a typical period of 30 min from ~2015 to 2105 UT. These variations were typically less than ~200 m/s and less than ~170 K. Furthermore, during the period from the first breakup to the end of the observation, the absolute values of LOS velocities of horizontal neutral winds and radar Doppler velocities showed a significant discrepancy; the baseline of the neutral wind variations was almost zero, whereas the baseline of the radar Doppler velocity variations was in the range of 100–300 m/s. However, the temporal variation of the neutral winds matched that of the radar Doppler velocities. For example, around 2330 UT before the second break up, the temporal negative excursion of neutral winds was similar to that of the radar Doppler velocities. Also, a significant increase in neutral temperature occurred around 2345 UT before the second breakup. Furthermore, from ~0000 to 0100 UT, the variations in neutral winds and radar Doppler velocities were associated with active auroras. In particular, from 2300 to 0100 UT, there were small-scale structures in the wind velocity distribution (indicated with red and blue colors). These complicated structures suggest the existence of local shear winds caused by Joule and particle heating.

[14] We applied the high-pass filter on the neutral winds and radar Doppler velocities to examine their relationship in detail. Figure 5 (top) is the same data as the third panel of Figure 3. The high-pass filtered temporal variations with frequencies less than one hour are shown in Figure 5 (bottom). Note that the temporal variation in neutral winds, usually less than 100 m/s, matched the variation in radar Doppler velocities from ~2130 to 0100 UT, even though

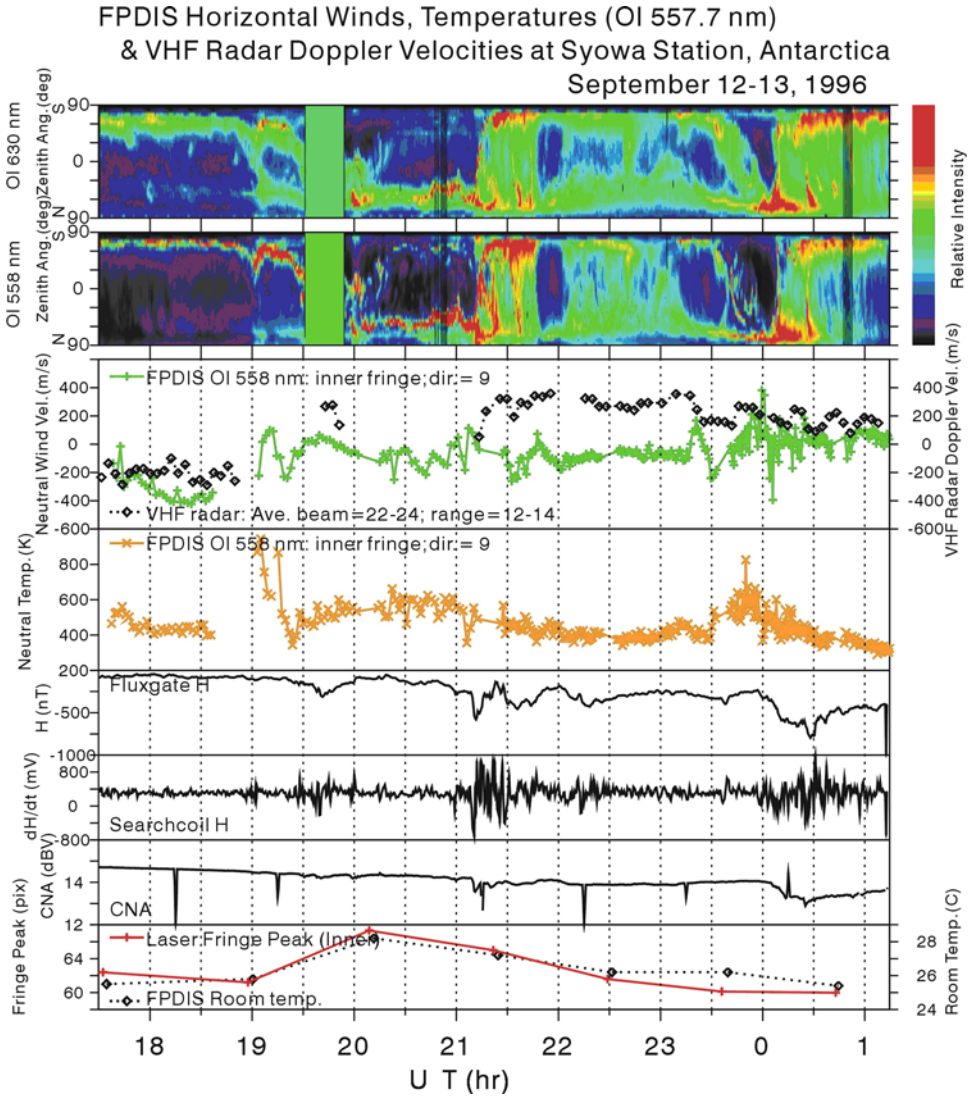

Figure 3. Summary plot of FPDIS, VHF radar, MSP, and geomagnetic observation data on 12–13 September 1996. The top two panels show MSP data of the OI 630-nm and OI 557.7-nm emissions. The third panel shows time variations of the LOS components of the horizontal neural wind and Doppler velocity in the *E* region at selected locations. The selected location of neutral wind data corresponds to the location of the Doppler velocity data. The fourth panel shows the time variation of neutral temperatures. The fifth and sixth panels show geomagnetic variations measured by fluxgate and searchcoil magnetometers, respectively. The seventh panel shows cosmic noise absorption data measured by a riometer. The bottom panel shows time variations of the peak position of the laser fringe and room temperature for monitoring the etalon spacing drift.

their absolute values were different during this period. The temporal variations were similar over a wide area of the FOVs. However, discrepancies appeared in the distant region around −74°S in latitude and 35°E in longitude. These similarities and differences will be discussed in section 4.2.

3.2. 11 September 1996 Case

[15] Auroral and geomagnetic conditions were also active on the night of 11 September. The K_p values were in the range between 3 and 5. For this event, the IMP8 satellite data was used for monitoring solar wind conditions since the WIND satellite was located in the magnetosphere. As shown in Figure 6, the IMF Bz was positive before ∼2200 UT, and turned negative around 2230 UT. The negative Bz condition probably persisted until ∼0020 UT, although there was no data from ∼2300 to 0010 UT. Figure 7 summarizes the FPDIS, VHF radar, auroral, and geomagnetic observations on this night. Auroral keograms obtained by MSP show stable auroral emissions from 1800 to 1900 UT. Unfortunately, MSP observed these emissions only in the zenith direction from ∼1910 to 2215 UT because of an operational problem. Panchromatic all-sky camera data (not shown) indicate that the equatorward motion of the auroral arc started at ∼2030 UT and that the first auroral breakup occurred around 2145 UT. This breakup also appears in the fluxgate

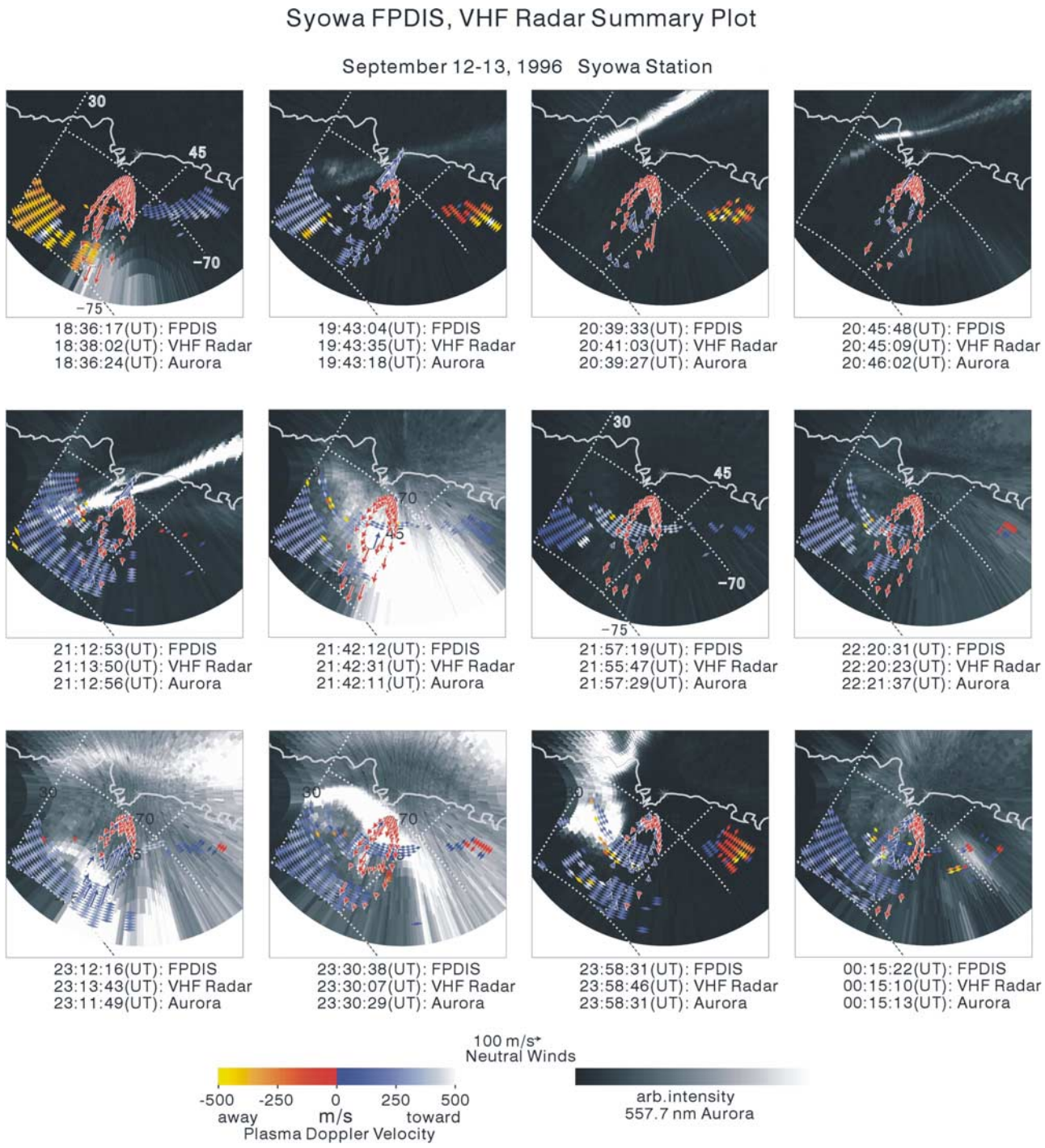

Figure 4. Summary plots of LOS components of horizontal neutral winds (arrows) and radar Doppler velocities (diamonds) superposed on the 557.7-nm auroral images obtained on 12–13 September 1996 in the geographical coordinate system. The location of Syowa is indicated by the cross. The LOS neutral wind velocities are indicated by the length of the arrow assuming an emission altitude of 120 km. Red indicates the wind direction is way from Syowa, and blue indicates it is toward Syowa. The radar Doppler velocity data are plotted in the area between −75° and −67° in latitude, 30° and 55° in east longitude with warm and cold colors representing the LOS drift directions away from and toward Syowa, respectively. The intensity of the 557.7 nm aurora image is arbitrary.

magnetometer data in Figure 7. Pulsating auroras subsequently appeared from ~2230 to 2340 UT, and the second auroral breakup occurred at ~0020 UT, as can be seen in MSP and fluxgate magnetometer data. Active auroral conditions continued till the end of the observation.

[16] Since the temperature of the observation room was rather stable on this night (see the plot at the bottom of

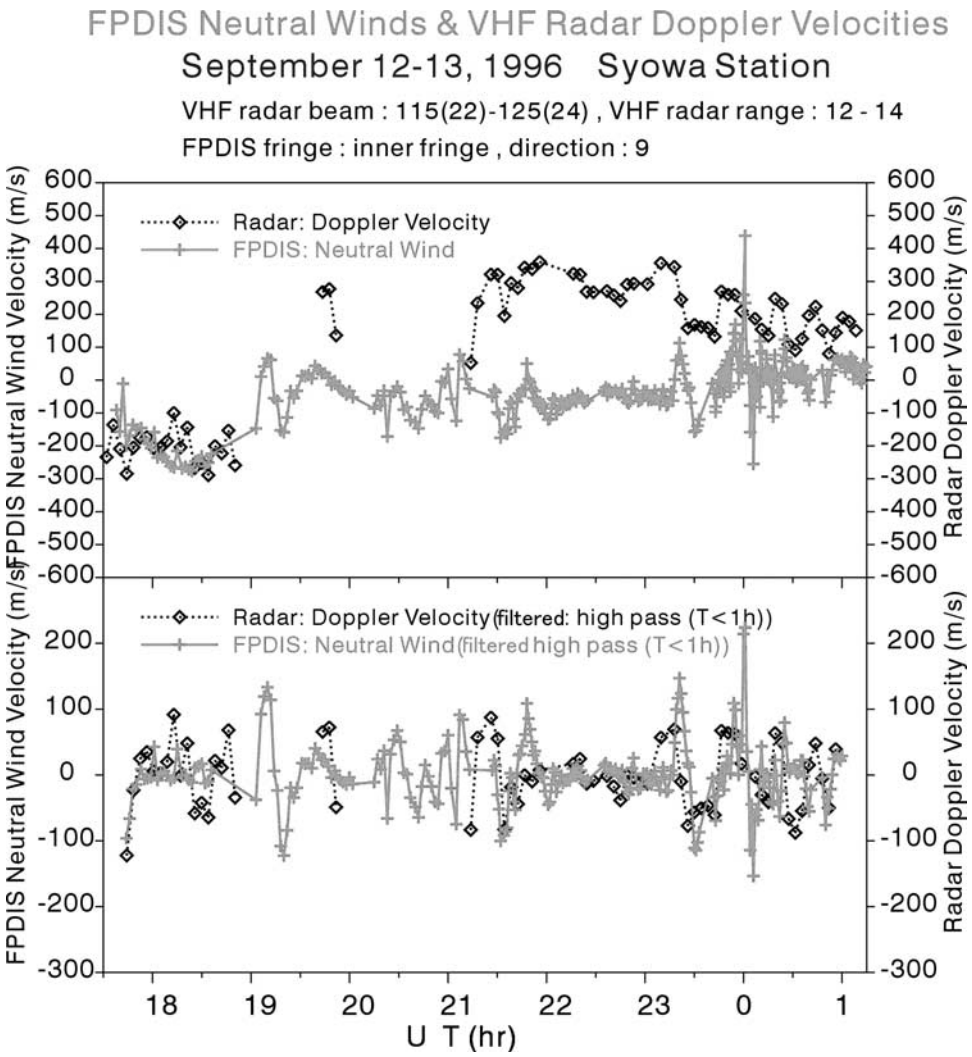

Figure 5. Relationship between LOS components of horizontal neutral wind velocities and radar Doppler velocities obtained on 12–13 September 1996. The top panel is the same as the third panel of Figure 3. The bottom panel shows the temporal variations of neutral winds and radar Doppler velocity processed with a high-pass filter (<1 hour). Plotted values are averages of the data for the selected locations indicated above the figure.

Figure 7), the etalon spacing drift could be corrected well. The temporal variations of the neutral winds, temperatures and radar Doppler velocities were similar to those obtained on 12–13 September, although echoes were not obtained by the VHF radar before ~2140 UT. When there were stable aurora emissions poleward of Syowa from ~1800 to 2000 UT, the LOS velocities of the neutral winds were away from Syowa at −50 and −140 m/s (negative). After the first breakup, the radar Doppler velocities were 200–400 m/s (positive), while the baseline the of neutral winds was almost zero. After the first breakup till the end of the observation, LOS velocities of the neutral winds and radar Doppler velocities had temporal variations with a period of less than ~1 hour. Figure 8 summarizes the neutral winds and radar Doppler velocity superposed on the 557.7-nm auroral images. The time variations of the neutral winds and radar Doppler velocities were similar over a wide area; from ~2258 to 0010 UT, the radar Doppler velocities in the poleward region were directed toward Syowa (cold colors), while in the eastward region, the radar Doppler velocities were away from Syowa (warm colors). After ~0030 UT, the region where the radar Doppler velocities were away from Syowa extended to south-eastward. The large-scale pattern of the radar Doppler velocities was consistent with the global two-cell convection pattern. In addition, Figure 8 reveals that neutral winds showed variations in time and space associated with auroral activity.

[17] To examine the relationship between the neutral winds and radar Doppler velocities in detail, we plotted the high-pass filtered temporal variations of the LOS components of horizontal neutral winds and radar Doppler velocities (Figure 9). Similar to the previous case, the temporal variation of the neutral winds with a period less than one hour showed very good agreement with that of the radar Doppler velocities from ~2200 to 0100 UT for variations with amplitudes less than ~100 m/s. Similar to

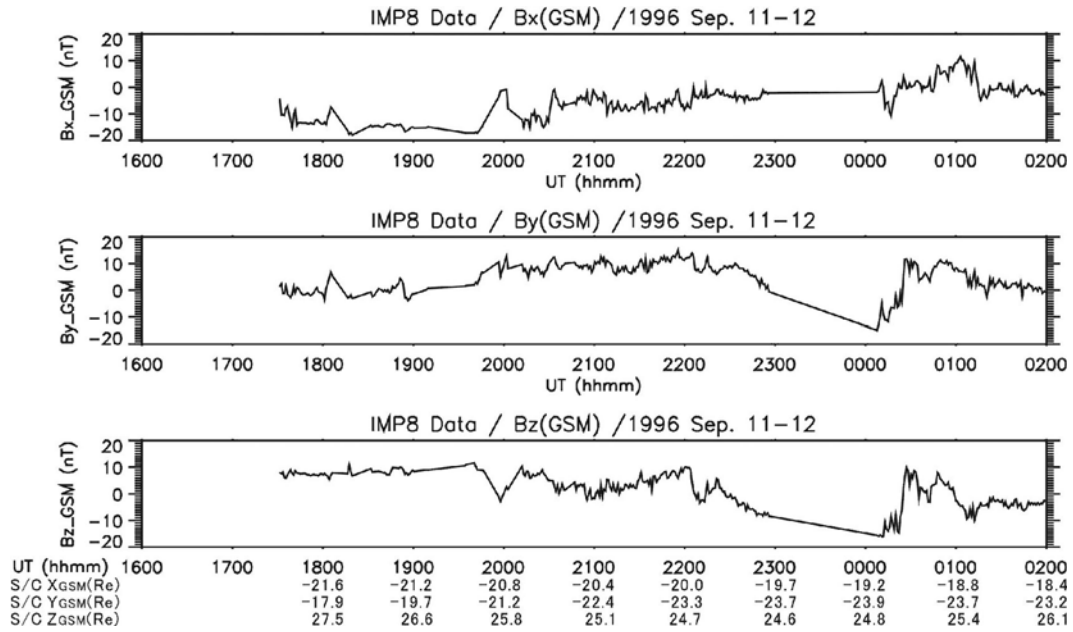

Figure 6. Solar wind conditions measured by the IMP8 satellite on 11–12 September of 1996.

the case of 12–13 September, the temporal variations occurred over a wide area of FOVs.

4. Discussion

[18] The two case studies revealed similar neutral wind and radar Doppler velocity variations with amplitudes less than 100 m/s and periods less than 1 hour. In section 4.1, we shall consider the error caused by the changes in emission peak altitude. In section 4.2, we shall quantitatively examine the relationship between the neutral wind and radar Doppler velocity. Finally, in section 4.3, we will discuss the mechanism that leads to their similarity.

4.1. Apparent Variations in Neutral Wind and Temperature due to Changes in OI 557.7-nm Emission Peak Altitude

[19] The peak altitude of the auroral OI 557.7-nm emission changes in the range of ~105–140 km, depending on the energy of precipitating electrons [e.g., *Holmes et al.*, 2005]. Since FPDIS observes neutral winds and temperatures around the emission peak altitude, apparent variations would occur if wind shear and temperature gradients existed in the vertical direction and the altitude of the emission peak changed. From previous observations and analyses of thermospheric models such as MSISE-90, these wind shears and temperature gradients generally exist in the *E* region [e.g., *Schunk and Nagy*, 2000]. Therefore the height variation of emission layer can introduce artifacts into their wind and temperature. Here we performed a careful analysis to discriminate between real and apparent variations in neutral wind and temperature as follows.

[20] First, we checked the negative excursion of the CNA intensity data since the negative excursion is caused by precipitation of high-energy electrons (E > ~20 keV) which causes a decrease in the altitude of the OI 557.7-nm emission. For example, typical negative excursions of CNA intensities occurred during ~2110–2120 UT on 12 September, ~0010–0025 UT on 13 September, 2145–2150 UT on 11 September, and 0020–0040 UT on 12 September. Though the FOV of the FPDIS was different from that of the riometer, which was pointed in the direction of the zenith, we can infer that the decrease in the peak altitude of the emission roughly corresponds to the decrease in the CNA intensity. Second, we examined the temporal variation of neutral temperatures. Since neutral temperatures generally decrease with decreasing altitude in the *E* region, a temporal and negative excursion would indicate a decrease in the peak altitude of the OI 557.7-nm emission. We found significant decreases in neutral temperatures (ΔTemp. = ~−100 to −200 K) at ~2105 UT and 2350 UT on 12 September and at 2150 UT on 11 September.

[21] The clear negative excursions of CNA intensities and neutral temperatures suggest that the emission peak altitude decreased, and therefore the apparent variation of neutral winds would be involved during these periods. However, these negative excursions occurred during rather few periods, e.g., ~2110 UT on 12 September and ~0010 UT on 13 September; most periods showed only a few negative excursions. The important point is that the similarity between neutral winds and the radar Doppler velocities cannot be explained by the apparent variations of neutral winds discussed here. Thus we conclude that the similarity between the neutral wind and radar Doppler velocity cannot be attributed to the changes in the emission altitude. Thus another mechanism would be needed to explain such a similarity.

4.2. Properties of the Variations of Neutral Wind and Radar Doppler Velocity Variation

[22] Here we examine the quantitative relationship between temporal variations in neutral winds and those in radar Doppler velocities whose timescale is less than 1 hour. First, the characteristics of the observed echo power are presented. Figure 10 shows the distributions of echo power on the nights of 12 and 11 September. Comparing the distributions of echo power shown in Figure 10 with the geometry of observation

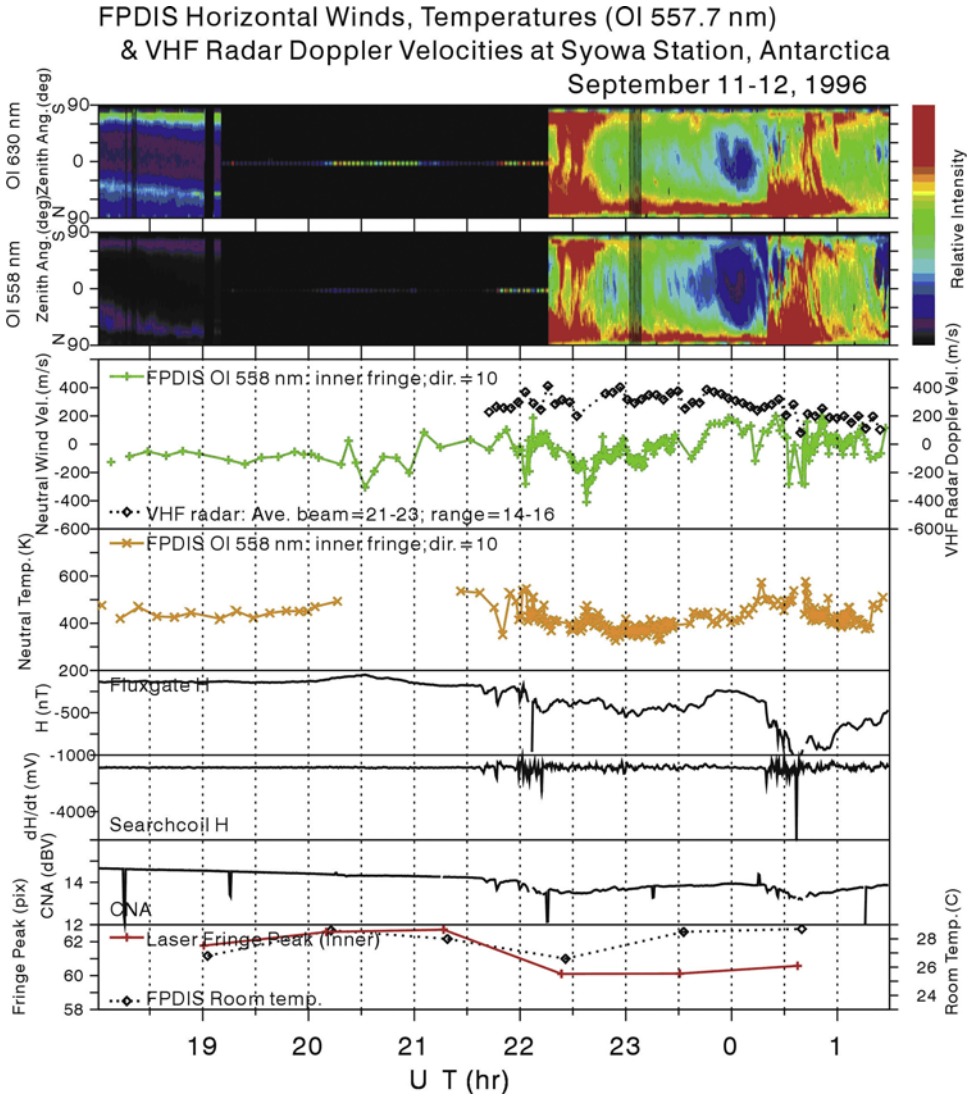

Figure 7. Summary plot of FPDIS, VHF radar, MSP, and geomagnetic observations on 11–12 September 1996. The format is the same as in Figure 3.

shown in Figure 1, we found that strong echoes were obtained mainly in two regions. One is the region where the raypath emitted from the radar is almost perpendicular to the geomagnetic field in the *E* region, that is, the aspect angle is almost zero, corresponding to the hatched area shown in Figure 1. Note that the hatched area extends toward both edges of the FOV because of the perpendicular conditions. Coherent radar echoes usually occur in this region [*Kustov et al.*, 2001]. Thus these echoes appeared across the middle of fringe positions and at the left edge of Figure 10 and are consistent with those in previous studies. Another region is the island-shaped echo region centered around −74°S in latitude and 43°E in longitude. The origin of these echoes is interesting, since the aspect angle is not zero at the altitude of *E* region [*Kustov et al.*, 2001]. A candidate for this island echo region is the reflection of the radar beam in the F region (T. Ogawa, private communication, 2002). To check for the possibility of the F region echoes, we calculated the relationship between aspect angles and altitudes in the FOV of the radar by assuming straight-line raypaths with the IGRF 95 geomagnetic model. Figure 11 shows the relationship between the FOV of FPDIS and the aspect angle of the VHF radar for assumed echo altitudes of 150 km, 175 km and 200 km. From these maps, we found that the zero-aspect angle condition is satisfied in the island echo region when the echo altitude is 175 km, which is lower than the altitude of the *F* region peak. The discrepancy between the estimated altitude of the echo region and that of the *F* region might be due to the low elevation angle of the radar transmission beam. In this case, since the elevation angle corresponding to the island echo region is ∼5°, the refraction of the transmitted beam would not be negligible, and it might cause an error in the estimation of the echo altitude. From the echo distributions in Figure 10, we also found that in the echoes in the zero-aspect angle region were more intense in the 11 September case, whereas the echoes in the island region were more intense in the 12 September case.

[23] Next, let us discuss the relationship between the neutral winds and radar Doppler velocities quantitatively. In each time series of neutral winds and radar Doppler velocities, only the temporal component whose period is less than 1 hour is used to make a scatterplot between temporal

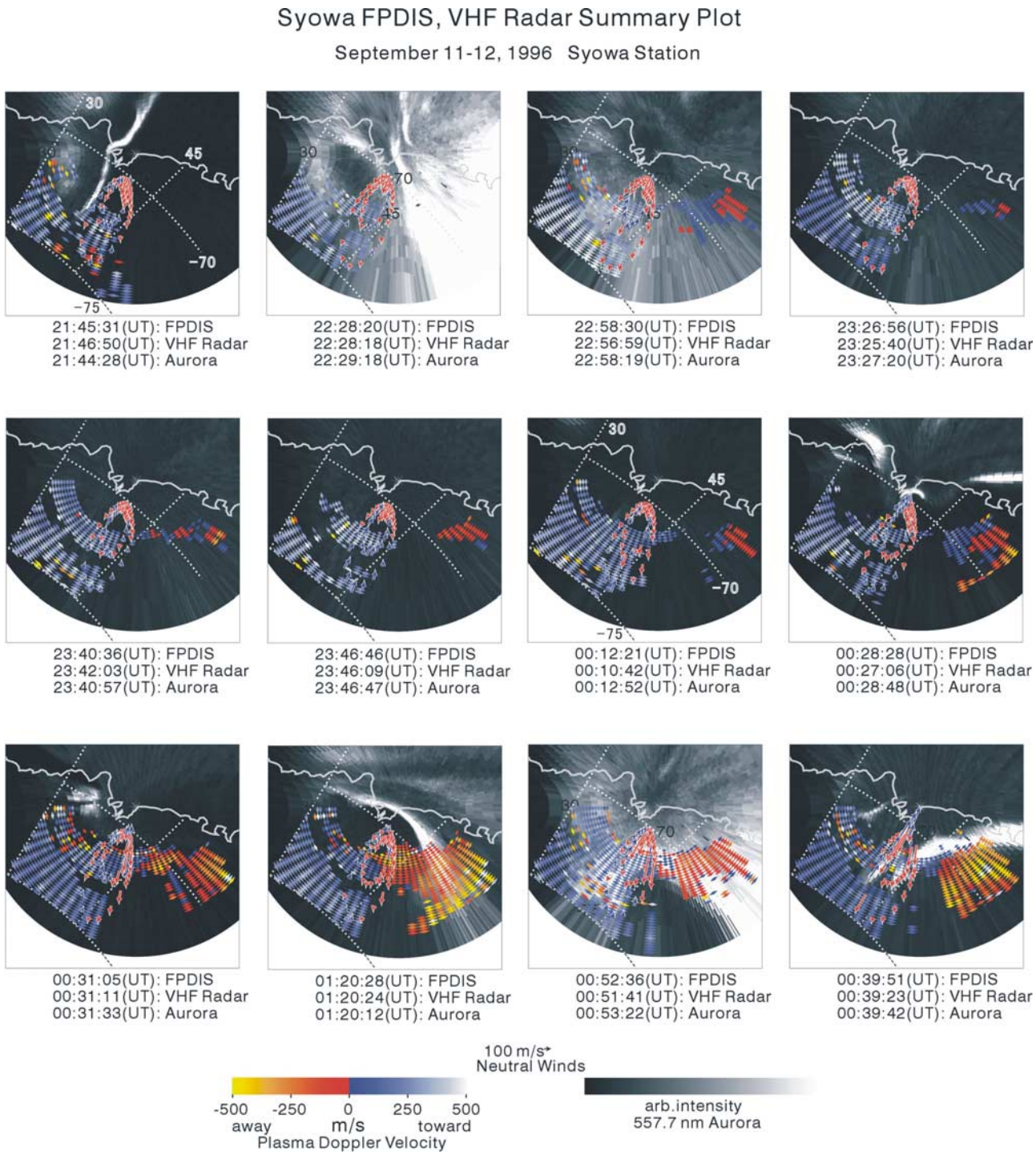

Figure 8. Summary plots of LOS components of horizontal neutral wind (arrows) and radar Doppler velocity (diamonds) superposed on the 557.7-nm auroral images obtained on 11–12 September 1996. The format is the same as in Figure 4.

variations of neutral winds and those of the radar Doppler velocities at the same location. Figures 12a and 12b are examples of scatterplots with good and rather bad correlations, respectively. The least squares method is used to fit a linear function to the scatterplot. The fitted function is $V_d = aU_n + b$, where V_d is the radar Doppler velocity, U_n is the neutral wind velocity, a is the inclination, and b is the intercept.

[24] From this fitting analysis, we obtained the values of the inclination, the correlation coefficient, and the covariance between the neutral wind and radar Doppler velocity at each data point on the inner and outer fringes of the FPDIS data. Figures 13 and 14 summarize these parameters for the 11–12 and 12–13 September cases. In both cases, the inner fringe data indicate that inclinations, correlation coefficients, and covariances have a double-peak structure, and that peaks

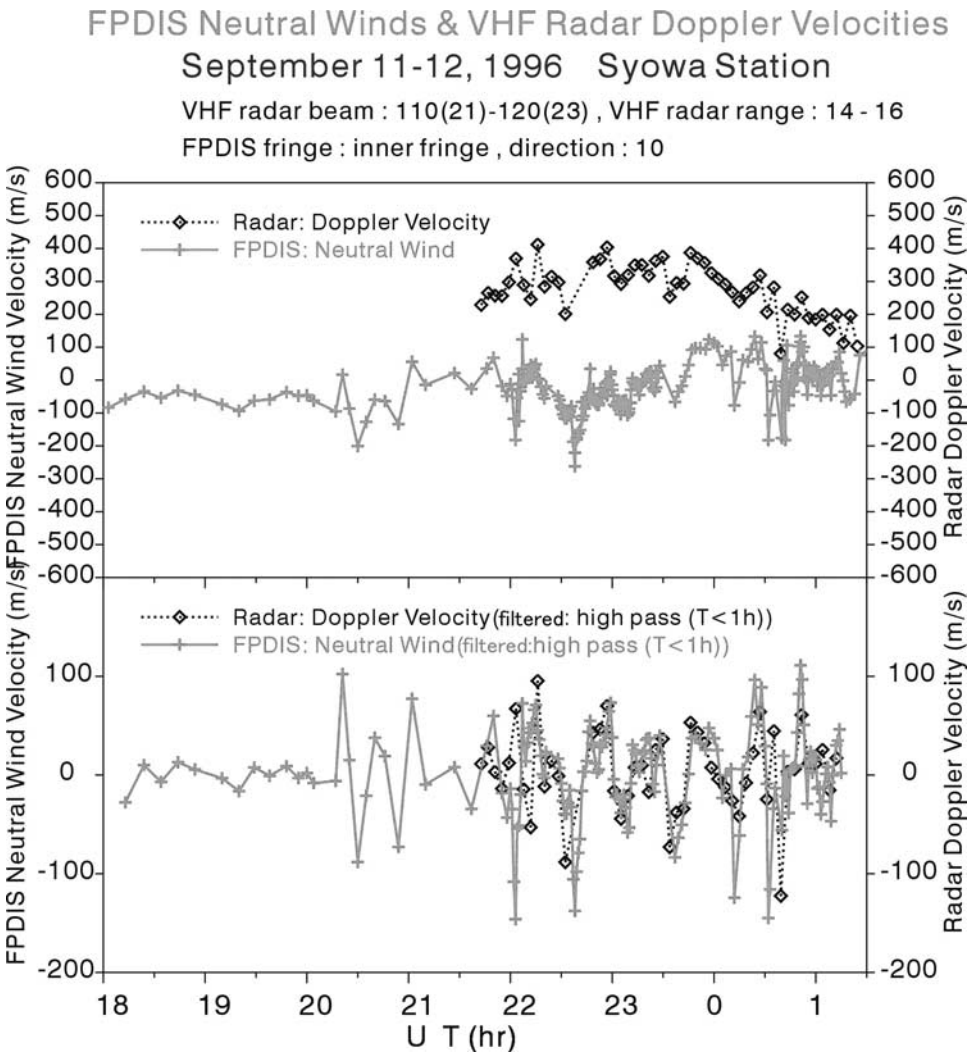

Figure 9. Relationship between LOS components of horizontal neutral wind velocities and radar Doppler velocities obtained on 11–12 September 1996. The format is the same as in Figure 5 except for the observation period.

appear at data points of 10 and 14. Comparing these values with the echo power distributions shown in Figure 10 makes it clear that the inclination, correlation coefficient, and covariance increases exactly correspond to the region where strong echoes occurred. Since the strong echo region appears across the FOV of the FPDIS, we obtained double-peak structures along the data points on the inner fringe, as shown in Figures 13a and 14a. In addition, the correlations at data points 9 and 10 on the inner fringe in the 11–12 September case were better than those in the 12–13 September case. The reason could be the difference in echo power shown in Figure 10, since the echo power in this region was more intense in the 11–12 September case.

[25] The correlations between the neutral wind and radar Doppler velocity were worse for the outer fringe data; the double-peak structure was not as clear as in the inner fringe data. It is noteworthy that the correlations were not good in the island echo region around −74°S in latitude and 43°E in longitude, even though the echo power was intense, especially for the 12–13 September case. The echo mechanism in the island region might be different from the normal echo mechanism in which the aspect angle is zero, and such a difference would be consistent with the interpretation that the echo from the island occurs in the *F* region. It would be interesting for a future experiment to investigate the possibility of *F* region echo by comparing VHF radar data with HF radar data.

4.3. Strong Coupling Between Neutrals and Ions in the E Region

[26] We showed that the temporal variations of neutral winds whose magnitudes were less than 100 m/s and whose periods were less than 1 hour matched the temporal variations of radar Doppler velocities in the region where strong echoes occurred except for the island-shaped echo region. These results suggest that it might be possible to estimate the distributions of neutral wind velocities from the VHF radar data. This would be advantageous since the VHF radar has a wider FOV than that of the FPDIS.

[27] The similarity between the neutral wind and radar Doppler velocity are probably caused by frequent collisions between neutrals and ions in the *E* region. The MSISE-90

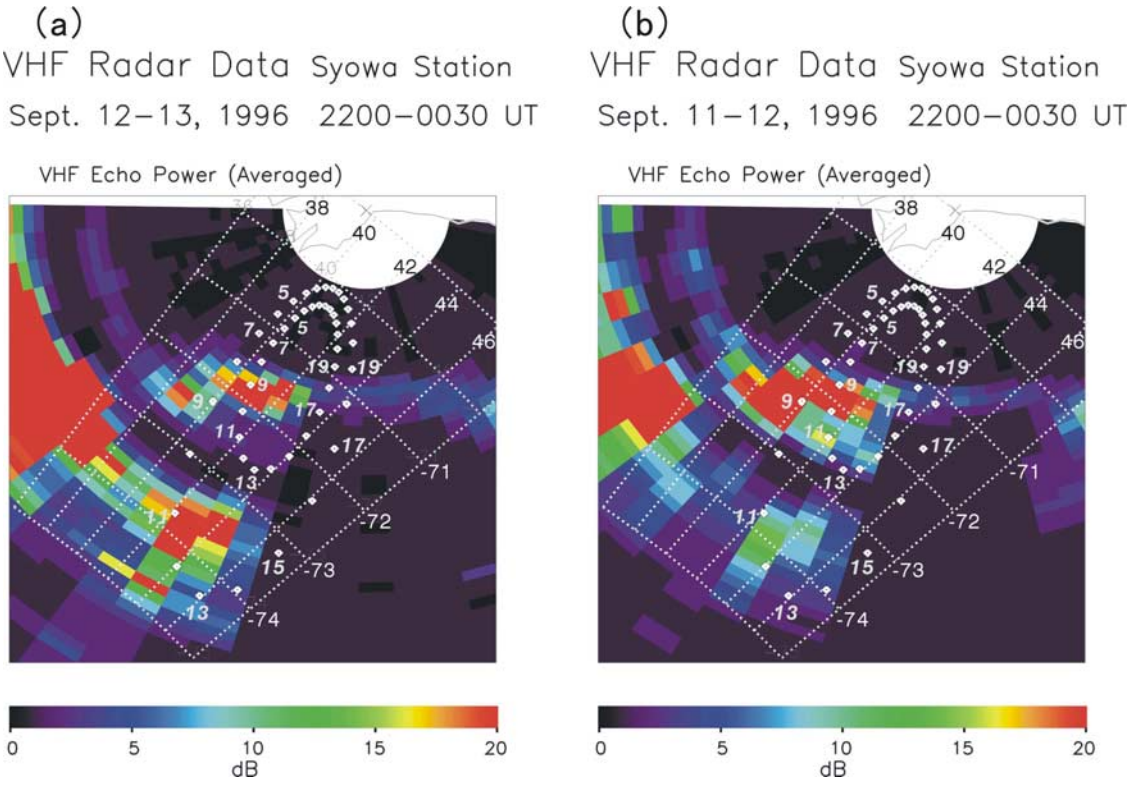

Figure 10. Geographical maps showing the distribution of average echo power during the periods of (a) 2200–0030 UT on 12–13 September 1996 and (b) 2200–0030 UT on 11–12 September 1996. Data points and data numbers for neutral winds are indicated by white diamonds and numerals, respectively.

and IRI-95 models give estimates of ion-neutral and neutral-ion momentum transfer frequencies at an altitude of 120 km to be 350 Hz for the neutral drag force, and 1.2×10^{-6} Hz for the ion drag force, respectively [*Schunk and Nagy*, 1980]. When we consider the collision between ions and neutrals, we obtain the momentum equation for ions as follows [*Nozawa and Brekke*, 1995]

$$m_i n_i \frac{d\mathbf{V_i}}{dt} = -m_i n_i \nu_{in}(\mathbf{V_i} - \mathbf{U}) \tag{1}$$

where m_i is the ion mass, n_i is the number density of ions, $\mathbf{V_i}$ and $\mathbf{U}$ are the ion and neutral velocities, respectively, ν_{in} is the ion-neutral momentum transfer frequency. The solution of above can be given by

$$\mathbf{V_i} = \mathbf{V_0}\exp(-\nu_{in}t) + \mathbf{U}[1 - \exp(-\nu_{in}t)]. \tag{2}$$

For a neutral wind velocity, similarly,

$$\mathbf{U} = \mathbf{U_0}\exp(-\nu_{ni}t) + \mathbf{V}[1 - \exp(-\nu_{ni}t)] \tag{3}$$

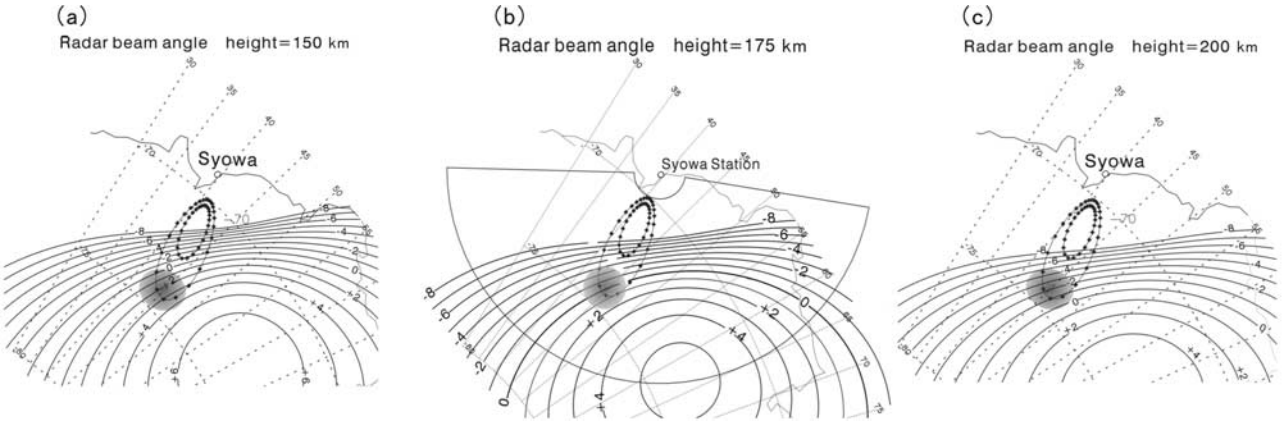

Figure 11. Relationship between the FOV of the FPDIS and the aspect angle of the VHF radar obtained by assuming straight line raypaths with the IGRF 95 geomagnetic model. Assumed echo altitudes are (a) 150 km, (b) 175 km, and (c) 200 km.

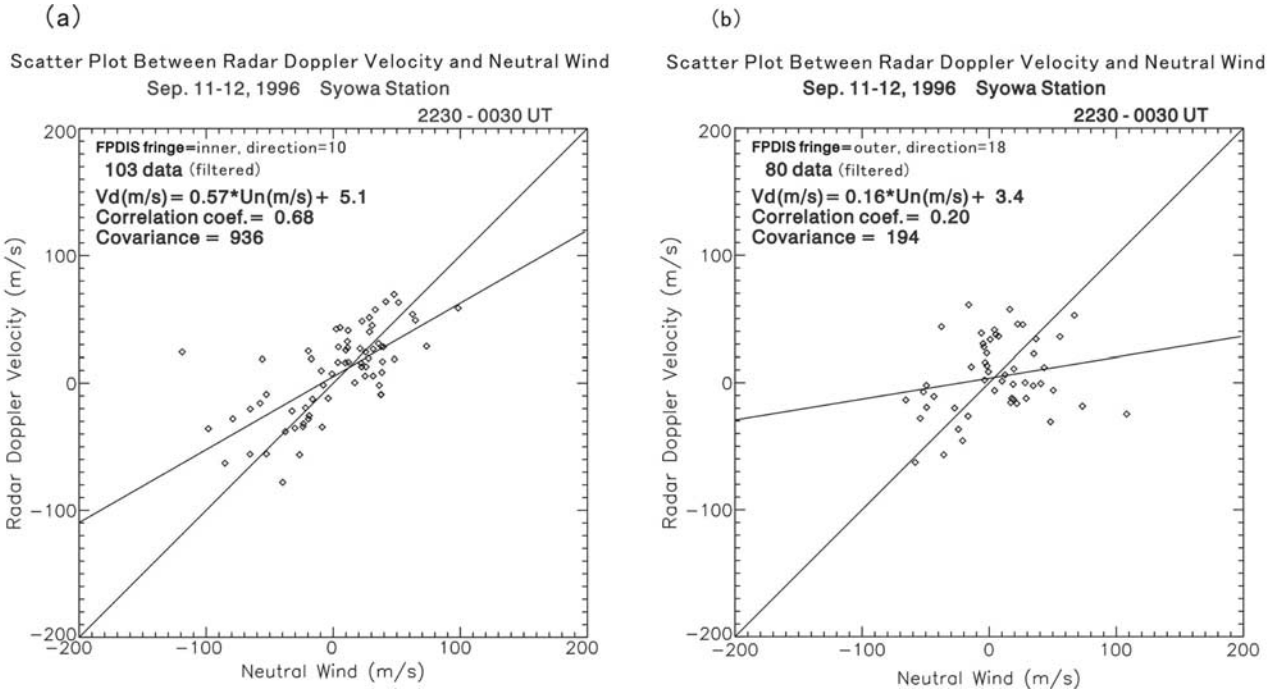

Figure 12. Examples of the scatterplots between neutral winds and the radar Doppler velocities measured at the same location when the correlations are (a) good and (b) bad.

where $\mathbf{V_0}$ and $\mathbf{U_0}$ are the ion and neutral velocities at t = 0. We therefore notice that the ion motion will approach a neutral wind velocity with a time constant given by

$$\tau_{in} = 1/\nu_{in}. \tag{4}$$

For neutral winds approaching a ion velocity, similarly,

$$\tau_{ni} = 1/\nu_{ni}. \tag{5}$$

These time constants τ_{in} and τ_{ni} are estimated to be 2.9×10^{-3} s and 8.3×10^5 s ($\sim$230 hr) from the collision frequencies described above.

[28] During a magnetically disturbed period, the electron number density and temperature show significant enhancements in the auroral *E* region. These enhancements can contribute to reduce the time constants between neutrals and ions. Since the data were obtained during the magnetically disturbed period, there is a possibility that the actual time constant of neutral winds driven by ions τ_{ni} is smaller than that estimated from the models. Based on EISCAT radar measurements during moderate to disturbed periods, *Nozawa and Brekke* [1995] showed the shorter time constants τ_{ni} in the range of 10^4–10^5 s (2.8–28 hr) in the *E* region. These time constants are likely still too large for the explanation of the temporal correlation between neutrals and ions (less than 1 hour) seen in this study. However, it is necessary to estimate quantitatively the neutral winds driven by ion drag force since the ion velocity is very large (e.g., $\sim$1000 m/s).

[29] Here we estimate the neutral wind driven by ion drag force by using equation (3). Assuming that the initial ion and neutral velocities are 1000 m/s and 0 m/s, respectively, and that the neutral-ion collision frequency is 1.2×10^{-6} Hz, the neutral wind driven by ions for 30 min is 2.2 m/s. However, the time constant should be shorter than that calculated from the models during the magnetically disturbed period as described above. In the shorter time constant case (10^4 s), that is, the neutral-ion collision frequency of 1×10^{-4} Hz [*Nozawa and Brekke*, 1995], the neutral wind driven by ions is 165 m/s after 30 min. Considering that 1000 m/s variation of ion velocity commonly occurs in the auroral ionosphere during a disturbed period, significant neutral winds can be driven by ion drag force with a period less than 1 hour with the shorter time constant. However, as seen in the data during the disturbed periods (see Figures 5 and 9), there are negative excursions in the absolute neutral winds, while the absolute rater Doppler velocities are always positive. It is impossible to generate the negative excursion of neutral winds by the positive ion velocities. In addition, the temporal variations of neutral winds would be different from those of ion velocities since the neutral velocity changes exponentially when the time constant is larger than the time variation seen in this study.

[30] Next we consider the ion motion driven by the neutral drag force. Since the time constant τ_{in} is small (2.9×10^{-3} s), the temporal variation of ions is expected to be almost identical to that of neutral for the period of 30 min to 1 hr. Therefore the similarity of temporal variation between neutrals and ions is easily produced by the neutral drag force. The amplitude of the temporal variation is less than 100 m/s. This fact is also consistent with the interpretation that the temporal ion motion is generated by the neutral drag force since the horizontal neutral winds with amplitude less than 100 m/s can be observed in the auroral *E* region. As discussed above, there is a possibility that the positive excursion of neutral winds is driven by the ion drag force. However, the negative excursion of neutral winds cannot be generated by the ion drag force, and the neutral velocity would change exponentially when the time constant is large. From above

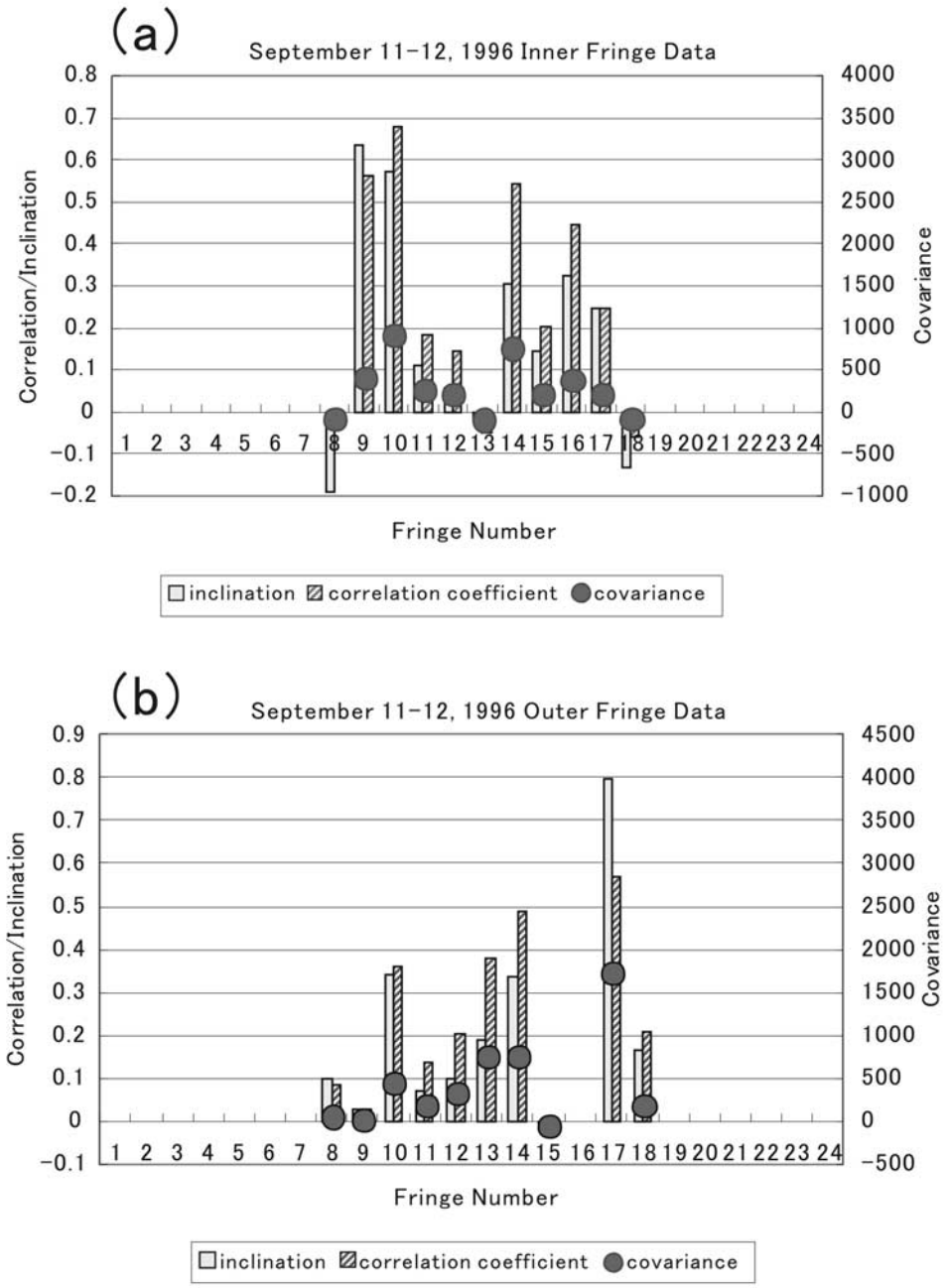

Figure 13. Histograms of inclination, correlation coefficient, and covariance of the relationship between neutral winds and radar Doppler velocities obtained on 11–12 September 1996 at (a) inner fringe data points and (b) outer fringe data points. Parameters cannot be estimated for data from 1 to 7 and from 19 to 23 because of the absence of radar echoes.

reason, it is probably reasonable to consider that the temporal variation between ions and neutrals is mainly caused by the neutral drag force for the cases measured in the disturbed periods. Another candidate for the cause might be the neutral dynamo, that is, the neutral-driven electric field. However, the neutral-driven electric field should be generated by neutral winds over the whole altitude range of the thermosphere whereas the FPDIS measures neutral winds in the certain altitude range, namely, the OI 557.7-nm emission layer.

[31] In this study, the neutral drag force probably generates concurrent variations with a quick response in the *E* region neutral wind and radar Doppler velocity. Therefore the neutral-ion coupling in the *E* region clearly contrasts with that in the F region where the ion drag force sometimes plays a role [*Thayer et al.*, 1995; *Sakanoi et al.*, 2002]. Regarding the driving force of neutral winds, their temporal variation may be driven by the pressure gradient force caused by local Joule heating, advection or thermospheric gravity waves associated with auroral substorms. However, the driving force of neutral winds will not be discussed here since it is rather difficult to estimate the effects of Joule heating and advection from observations at Syowa. In the following, we will explain similar variations in neutral wind and radar

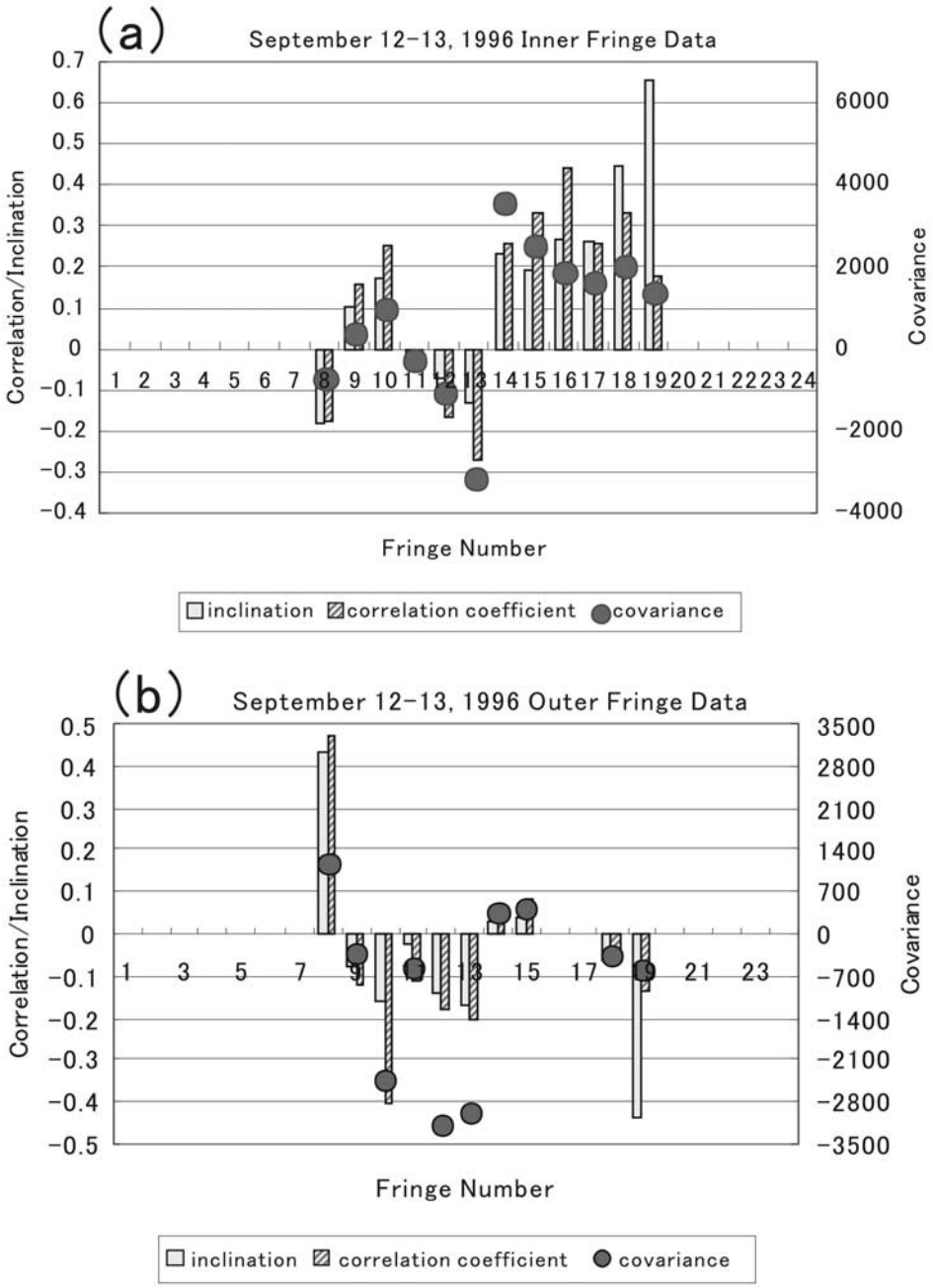

Figure 14. Same as Figure 13, but for the case of 12–13 September 1996. Parameters cannot be estimated for data from 1 to 7 and from 20 to 23 because of the absence of radar echoes.

Doppler velocity by using the theory of field-aligned irregularities in the *E* region.

[32] There are many studies on the generation of field-aligned irregularities in the *E* region and their relationship to VHF radar measurement data [e.g., *Fejer and Kelly*, 1980]. Many researchers have reported that gradient drift instability occurs if the **E** × **B** drift speed is less than the ion acoustic speed of 300–450 m/s [e.g., *Nielsen and Schlegel*, 1983, 1985]. In this case, the linear theory of electrostatic waves can be applied to the irregularity, and the phase velocity of the irregularity is almost equal to the **E** × **B** drift speed. The radar Doppler velocity is determined from a type-2 echo. Accordingly, the radar Doppler velocities correspond to the line-of-sight component of the **E** × **B** drift speed. If the **E** × **B** drift speed exceeds the ion acoustic speed, nonlinear instabilities such as the two-stream instability and/or Farley-Bunneman instability are dominant and in most cases, the phase velocity of the irregularity does not correspond to the **E** × **B** drift speed. The VHF radar would observe a type 1 echo, and the radar Doppler velocities would saturate around the ion acoustic speed.

[33] Thus the interpretation of variations in radar Doppler velocities depends on the magnitude of the **E** × **B** drift speed. However, unfortunately, the **E** × **B** drift data were not available during the period of the present study. The absolute values of observed radar Doppler velocities were in the range

of ~300–400 m/s when the temporal variation of the neutral winds was similar to that of the radar Doppler velocities, as shown in Figures 5 and 9. Since these velocities are close to the ion acoustic speed (~420 m/s) estimated from the MSISE-90 and IRI-95 models, we speculate that the observed radar Doppler velocities saturated at the ion acoustic speed because of the Farley-Bunemann/two stream instability, and that the actual $\mathbf{E} \times \mathbf{B}$ drift speeds exceeded the local ion acoustic speed. If this interpretation is correct, we cannot discuss the observed radar Doppler velocities by using the linear theory of inospheric irregularities. However, as the first step, we shall interpret the good correlation between the neural winds and radar Doppler velocities on the basis of the linear theory. Afterward, we will briefly discuss the case in which the $\mathbf{E} \times \mathbf{B}$ drift speeds are greater than the ion acoustic speed.

[34] From the momentum equations of electrons and ions, and the their continuity equation, the frequency ω_r and the growth rate Γ of fluctuations are given by [*Fejer and Kelly*, 1980; *Tanaka and Venkateswaran*, 1982a, 1982b]

$$\omega_r = [\mathbf{k} \cdot (\mathbf{V_e} + \Psi \mathbf{V_i})]/(1 + \Psi) \tag{6}$$

$$\Gamma = (1+\Psi)^{-1}\left\{\frac{\Psi}{\nu_{in}}\left[(\omega_r - \mathbf{k}\cdot\mathbf{V_i})^2 - k^2 C_S^2\right] + \frac{1}{L_N}\left[(\omega_r - \mathbf{k}\cdot\mathbf{V_i})(\nu_{in}k_y/\Omega_i)\right]\right\} - 2\alpha N_0 \tag{7}$$

where $\mathbf{k}$ is the wave number vector, $\mathbf{V_e}$ and $\mathbf{V_i}$ are the velocities of electrons and ions, respectively, $\Psi = \Psi_0(k_\perp^2/k^2 + \Omega_e^2 k_\parallel^2/\nu_e k^2)$, where $\Psi_0 = \nu_e\nu_i/\Omega_e\Omega_i$, C_S is the ion acoustic speed, ν_{in} is the ion-neutral collision frequency, $L_N = N(\partial N/\partial z)^{-1}$ is the vertical electron density gradient length, α is the recombination coefficient ($\sim 3 \times 10^7$ cm^3/s), and N_0 is the background electron density. Here we assume that the $\mathbf{E} \times \mathbf{B}$ drift speed is less than the ion acoustic speed. In this case, the following relation can be applied.

$$\mathbf{k} \cdot (\mathbf{V_e} - \mathbf{V_i}) < C_S(1 + \Psi) \approx 300 - 500\,\mathrm{m/s} \tag{8}$$

[35] In this way, we obtain a linear theory of the irregularity. Considering the strong coupling between neutrals and ions in the *E* region, the phase velocity of the irregularity can be derived as

$$\mathbf{V_d} = \frac{1}{1+\Psi}\frac{\mathbf{E}\times\mathbf{B}}{B_0^2} + \frac{\Psi}{1+\Psi}\mathbf{U}_\perp + \mathbf{U}_\parallel = \frac{1}{1+\Psi}\frac{\mathbf{E}\times\mathbf{B}}{B_0^2} + \left(\frac{\Psi}{1+\Psi}\sin\theta + \cos\theta\right)\mathbf{U} \tag{9}$$

where $\mathbf{U}$ is the neutral wind velocity, and θ is the inclination of the geomagnetic field. Considering that Ψ is estimated to be 3×10^{-3} using the MSISE-90 model, and θ is 63.5°at Syowa, equation (9) simplifies to

$$\mathbf{V_d} \approx \frac{\mathbf{E}\times\mathbf{B}}{B_0^2} + 0.45\mathbf{U} = \mathbf{V_e} + 0.45\mathbf{U} \tag{10}$$

and, therefore the relation in the LOS direction is given by

$$V_{dLOS} \approx V_{eLOS} + 0.45 U_{LOS} \tag{11}$$

where the subscript *LOS* indicates the component in the LOS direction.

[36] On the other hand, as seen from the time variations of absolute values of neutral winds and radar Doppler velocities during the periods from 2130 on 12 September to 0100 UT on 13 September, and from 2130 on 11 September to 0100 UT on 12 September shown in the top panels of Figures 5 and 9, the observed relationship between neutral winds and radar Doppler velocities would be expressed as

$$V_{dLOS} \approx \beta + \alpha U_{LOS} \tag{12}$$

where α and β are constants. There is a linear relationship between the temporal variations between the neutral wind and radar Doppler velocity, (see Figure 12a), and the inclination is estimated (see Figures 13 and 14). For the data during the period mentioned above, it is likely that α practically equals the inclination. We found that the observed inclinations α are in the range of 0.3–0.8 when the correlation coefficients are greater than 0.5. As seen from Figures 5 and 9, there are significant offset between the absolute values of the neutral winds and those of the radar Doppler velocities (350–400 m/s), and this would correspond to the constant β. The theoretical formula (equation (11)) is similar to the observed relation (equation (12)). Therefore it seems that the observed similarity between neutral wind and radar Doppler velocity is consistent with the linear theory.

[37] However, there are unsolved problems as follows. Firstly, the values of observed inclinations α were sometimes rather greater than the theoretical inclination 0.45. As shown in Figures 13 and 14, the maximum value of observed inclination reached 0.8 on the outer fringe data for the 12 September case. In addition, the inclinations were more than 0.6 at two data points in the inner fringe data. Secondly, the values of β were almost constant in the range of 350–400 m/s from observation data during the period from 2130 on 12 September to 0100 UT on 13 September, and from 2130 on 11 September to 0100 UT on 12 September. This fact implies that the electron $\mathbf{E} \times \mathbf{B}$ drift velocities were almost constant even though significant substorms occurred during these periods since β corresponds to that of the LOS component of the electron $\mathbf{E} \times \mathbf{B}$ drift velocity, from equations (11) and (12). However, the $\mathbf{E} \times \mathbf{B}$ drift velocities generally show large variations during substorms. Thirdly, it is likely that the $\mathbf{E} \times \mathbf{B}$ drift speed exceeded the ion acoustic speed since the absolute values of the radar Doppler velocities were almost constant (350–400 m/s) during the periods when the similar variations of neutral winds and radar Doppler velocities occurred. These values are close to the ion acoustic speed of 420 m/s. If the $\mathbf{E} \times \mathbf{B}$ drift speeds exceeded the ion acoustic speed in the two cases used in this study, we cannot apply the linear theory of instabilities as discussed above.

[38] In the case that the $\mathbf{E} \times \mathbf{B}$ drift speed exceeds the ion acoustic speed, a numerical analysis would be needed to examine the nonlinear characteristics of the instabilities and their relation to neutral winds [*Fejer and Kelly*, 1980].

However, such an investigation is beyond the scope of the present study. To clarify the problems discussed above, an independent $\mathbf{E} \times \mathbf{B}$ drift observation would be needed; in particular, simultaneous measurements using SuperDARN HF radars, auroral VHF radar, and Fabry-Perot imager would be useful for gaining an understanding of the precise neutral-ion coupling processes in the *E* region.

5. Conclusions

[39] We examined the precise relationship between neutral wind and the radar Doppler velocity in the *E* region on 11–12 and 12–13 September 1997 by using data obtained by a Fabry-Perot Doppler imaging system and auroral VHF radar at Syowa Station, Antarctica. Our findings are summarized as follows.

[40] 1. From the FPDIS 557.7 nm data and the VHF radar Doppler velocity data obtained on 11 and 12 September 1996, we found that the temporal variations of neutral winds in the *E* region agree well with those of radar Doppler velocities. The magnitudes of temporal components in neutral winds and radar Doppler velocities are less than 100 m/s, and the periods are less than one hour. On the other hand, the absolute values of line-of-sight velocities are around zero for the neutral winds are about 350–400 m/s for the radar Doppler velocities.

[41] 2. The correlation coefficients, covariances and inclinations of temporal variation in the neutral wind and radar Doppler velocity were estimated by using a linear function fitting on scatterplots. The parameters had maximum values in the region where strong echoes (> 20 dB) occurred. Thus it might be possible to estimate practically temporal variations of neutral winds from VHF radar data obtained with the strong echoes. It is necessary to verify this possibility theoretically and observationally in the future studies. The correlations are not good in the island-shaped echo region around −74°S in latitude and 43°E in longitude, suggesting that these echoes occur in the lower *F* region.

[42] 3. Considering that the typical periods of the velocity variations are less than one hour, and that the neutral-ion and ion-neutral momentum transfer collision frequencies in the *E* region are $\sim 10^{-6}$ Hz and $\sim 10^{2}$ Hz, respectively, we suggest that the neutral drag force produces the good correlation between the temporal variations in neutral winds and those in radar Doppler velocities.

[43] 4. The linear theory of *E* region irregularities predicts a linear relationship between the radar Doppler velocity and the neutral wind velocity, and the observed relationship is consistent with the linear theory. However, there is a possibility that the $\mathbf{E} \times \mathbf{B}$ drift speed exceeds the ion acoustic speed (∼420 m/s) since the absolute values of radar Doppler velocities are almost constant (350–400 m/s) during the periods of correlated variations. In this case, nonlinear processes such as the Farley-Bunneman instability would become dominant in the *E* region, and we cannot apply the linear theory to the observed temporal variations. The investigation on the nonlinear characteristics of instabilities is beyond the scope of the present study. To resolve these problems, an independent $\mathbf{E} \times \mathbf{B}$ drift observation should be undertaken; in particular, simultaneous measurements using SuperDARN HF radars, auroral VHF radar, and Fabry-Perot imager would be useful for gaining an understanding of the precise neutral-ion coupling processes in the *E* region.

[44] **Acknowledgments.** We thank all the members of the 37th wintering party of the Japanese Antarctic Research Expedition for their support at Syowa Station. MSP and Geomagnetic data were provided by the World Data Center-C2 for Aurora at the National Institute of Polar Research. IMF conditions measured by WIND and IMP8 were downloaded from the "cdaweb" service site at the URL http://cdaweb.gsfc.nasa.gov/cdaweb/istp_public. The MSISE-90 and IRI-95 models were obtained from the Web pages of NASA's National Space Science Data Center.

[45] Zuyin Pu thanks Kazuo Shiokawa and another reviewer for their assistance in evaluating this paper.

References

Aruliah, A. L., E. M. Griffin, A. D. Aylward, E. A. K. Ford, M. Kosch, C. J. Davis, V. S. C. Howells, S. E. Pryse, H. R. Middleton, and J. Jussila (2005), First direct evidence of meso-scale variability on ion-neutral dynamics using co-located tristatic FPIs and EISCAT radar in Northern Scandinavia, *Ann. Geophys.*, *23*, 147–162.

Cierpka, K., M. J. Kosch, M. Rietveld, K. Schlegel, and T. Hagfors (2000), Ion-neutral coupling in the high-latitude F-layer from incoherent scatter and Fabry-Perot interferometer measurements, *Ann. Geophys.*, *18*, 1145–1153.

Conde, M., and R. W. Smith (1998), Spatial structure in the thermospheric horizontal wind above Poker Flat, Alaska, during solar minimum, *J. Geophys. Res.*, *103*(A5), 9449–9471.

Conde, M., et al. (2001), Assimilated observations of thermospheric winds, the aurora, and ionospheric currents over Alaska, *J. Geophys. Res.*, *106*, 10,493–10,508.

Deng, W., T. L. Killeen, A. G. Burns, and R. G. Roble (1991), The flywheel effect: Ionospheric currents after a geomagnetic storm, *Geophys. Res. Lett.*, *18*, 1845–1848.

Deng, W., T. L. Killeen, A. G. Burns, R. G. Roble, J. A. Slavin, and L. E. Wharton (1993), The effects of neutral inertia on ionospheric currents in the high-latitude thermosphere following a geomagnetic storm, *J. Geophys. Res.*, *98*, 7775–7790.

Fejer, B. G., and M. C. Kelly (1980), Ionospheric irregularities, *Rev. Geophys.*, *18*, 401–454.

Fujii, R., S. Nozawa, N. Matuura, and A. Brekke (1998a), Study on neutral winds contribution to the electrodynamics in the polar ionosphere using EISCAT CP-1 data, *J. Geophys. Res.*, *103*, 14,731–14,739.

Fujii, R., S. Nozawa, S. C. Buchert, N. Matuura, and A. Brekke (1998b), The motion of ions in the auroral ionosphere, *J. Geophys. Res.*, *103*, 20,685–20,695.

Fuller-Rowell, T. J., M. V. Codrescu, R. J. Moffett, and S. Quegan (1994), Response of the thermosphere and ionosphere to geomagnetic storms, *J. Geophys. Res.*, *99*, 3893–3914.

Haldoupis, C., and E. Nielsen (1989), Very large phase velocities of non two-stream, meter scale irregularities in the high latitude E region ionosphere, *J. Geophys. Res.*, *94*, 13,489–13,504.

Holmes, J. M., M. Conde, C. Deehr, and D. Lummerzheim (2005), Morphology of evening sector aurorae in ramda-557.7-nm Doppler temperatures, *Geophys. Res. Lett.*, *32*, L02103, doi:10.1029/2004GL021553.

Igarashi, K., K. Ohtaka, M. Kunitake, T. Tanaka, and T. Ogawa (1995), Development of scanning beam VHF auroral radar system (extended abstract), *Proc. NIPR Symp. Upper Atoms. Phys.*, *8*, 69–73.

Ishii, M., S. Oyama, S. Nozawa, R. Fujii, E. Sagawa, S. Watari, and H. Shinagawa (1999), Dynamics of neutral wind in the polar region observed with two Fabry-Perot interferometers, *Earth Planet. Sci.*, *51*, 833–844.

Killeen, T. L., and R. G. Roble (1988), Thermospheric dynamics: Contributions from the first 5 years of the Dynamics Explorer program, *Rev. Geophys.*, *26*, 329–367.

Killeen, T. L., R. A. Heelis, P. B. Hays, N. W. Spencer, and W. B. Hanson (1985), Neutral motions in the polar thermosphere for northward interplanetary magnetic field, *Geophys. Res. Lett.*, *12*, 159–162.

Kosch, M. J., K. Cierpka, M. T. Rietveld, T. Hagfors, and K. Schlegel (2001), High-latitude ground-based observations of the thermospheric ion-drag time constant, *Geophys. Res. Lett.*, *28*, 1395–1398.

Kustov, A. V., K. Igarashi, D. Andre, K. Ohtaka, N. Sato, H. Yamagishi, and A. Yukimatu (2001), Observations of 50- and 12-MHz auroral coherent echoes at the Antarctic Syowa station, *J. Geophys. Res.*, *106*, 12,875–12,888.

Nakajima, H., S. Okano, H. Fukunishi, and T. Ono (1995), Observations of thermospheric wind velocities and temperatures by the use of a Fabry-Perot Doppler imaging system at Syowa Station, Antarctica, *Appl. Opt.*, *34*, 8382–8395.

Nielsen, E., and K. Schlegel (1983), A first comparison of STARE and EISCAT electron drift velocity measurements, *J. Geophys. Res.*, *88*, 5745–5750.

Nielsen, E., and K. Schlegel (1985), Coherent radar Doppler measurements and their relationship to the ionospheric electron drift velocity, *J. Geophys. Res.*, *90*, 3498–3504.

Nielsen, E., M. Uspenskii, A. Kustov, A. Huuskonen, and J. Kangas (1988), On the dependence of the Farley-Buneman turbulence level on ionospheric electric field, *J. Atmos. Terr. Phys.*, *50*, 601–605.

Nozawa, S., and A. Brekke (1995), Studies of the *E* region neutral wind in the disturbed auroral ionosphere, *J. Geophys. Res.*, *100*, 14,717–17,734.

Ogawa, T. (1996), Radar observations of ionospheric irregularities at Syowa Station, Angarctica: A brief overview, *Ann. Geophys.*, *14*, 1454–1461.

Rees, D., A. L. Aruliah, T. J. Fuller-Rowell, A. D. Farmer, and K. S. C. Freeman (1991), Long-lived polar thermospheric vortices: A combined radar and optical study, *J. Atmos. Terr. Phys.*, *53*, 493–514.

Ridley, A. J., A. D. Richmond, T. I. Gombosi, D. L. Zeeuw, and C. R. Clauer (2003), Ionospheric control of the magnetospheric configuration: Thermospheric neutral winds, *J. Geophys. Res.*, *108*(A8), 1328, doi:10.1029/2002JA009464.

Sakanoi, T., H. Fukunishi, S. Okano, N. Sato, H. Yamagishi, and A. S. Yukimatu (2002), Dynamical coupling of neutrals and ions in the high-latitude F region: Simultaneous FPI and HF radar observations at Syowa Station, Antarctica, *J. Geophys. Res.*, *107*(A11), 1388, doi:10.1029/2001JA007530.

Schlegel, K. (1996), Coherent backscatter from ionospheric E-region plasma irregularities, *J. Atmos. Terr. Phys.*, *58*, 933–941.

Schunk, R. W., and A. F. Nagy (1980), Ionospheres of the terrestrial planets, *Rev. Geophys.*, *18*, 813–852.

Schunk, R. W., and A. F. Nagy (2000), *Ionospheres: Physics, Plasma Physics and Chemistry*, Cambridge Univ. Press, Cambridge, U. K.

Tanaka, T., and S. V. Venkateswaran (1982a), Characteristics of field-aligned E-region irregularities over Iioka (36°N), Japan-I, *J. Atmos. Terr. Phys.*, *44*, 381–393.

Tanaka, T., and S. V. Venkateswaran (1982b), Characteristics of field-aligned E-region irregularities over Iioka (36°N), Japan-II, *J. Atmos. Terr. Phys.*, *44*, 395–406.

Thayer, J. P. (1998), Height-resolved Joule heating rates in the high latitude E-region and influence of neutral winds, *J. Geophys. Res.*, *103*, 471–487.

Thayer, J. P., G. Crowley, R. H. Niciejewski, T. L. Killeen, J. Buchau, and B. W. Reinisch (1995), Ground-based observations of ion/neutral coupling at Thule and Qanaq, Greenland, *J. Geophys. Res.*, *100*, 12,189–12,199.

Wang, W., A. G. Burns, and T. L. Killeen (2006), A numerical study of the response of ionospheric electron temperature to geomagnetic activity, *J. Geophys. Res.*, *111*, A11301, doi:10.1029/2006JA011698.

H. Fukunishi, Japan Society for the Promotion of Science Beijing Office, 616 Library of Chinese Academy of Sciences, 33 Beisihuan Xilu, Zhongguancun, Beijing 100190, China. (fuku@pat.geophys.tohoku.ac.jp)

K. Igarashi, National Institute of Information and Communications Technology, 4-2-1 Nukui-kitamachi, Koganei 184-8795, Japan. (igarashi@nict.go.jp)

N. Nishitani, Solar-Terrestrial Environment Laboratory, Nagoya University, Furo-cho, Chikusa-ku, Nagoya 464-8601, Japan. (nisitani@stelab.nagoya-u.ac.jp)

S. Okano and T. Sakanoi, Graduate School of Science, Tohoku University, Aramaki-aza-aoba, Aoba, Sendai 980-8578, Japan. (okano@pparc.geophys.tohoku.ac.jp; tsakanoi@pparc.geophys.tohoku.ac.jp)